Implications for the geometry of plate boundaries in NE Asia based on the geodetic analysis of the 2020 Mw 6.4 Koryak event

Article *in* Geophysical Journal International · March 2023

DOI: 10.1093/gji/ggad142

CITATIONS
0

READS
44

6 authors, including:

Nikos Svigkas
National Institute of Geophysics and Volcanology
22 PUBLICATIONS **144** CITATIONS
SEE PROFILE

Simone Atzori
National Institute of Geophysics and Volcanology
129 PUBLICATIONS **2,418** CITATIONS
SEE PROFILE

Andrey Kozhurin
Institute Of Volcanology And Seismology
47 PUBLICATIONS **655** CITATIONS
SEE PROFILE

C. Tolomei
National Institute of Geophysics and Volcanology
135 PUBLICATIONS **1,922** CITATIONS
SEE PROFILE

Geophysical Journal International

Geophys. J. Int. (2023) **234,** 1412–1421
Advance Access publication 2023 March 30
GJI Seismology

https://doi.org/10.1093/gji/ggad142

Implications for the geometry of plate boundaries in NE Asia based on the geodetic analysis of the 2020 M_w 6.4 Koryak event

Nikos Svigkas [1], Simone Atzori,[1] Andrey Kozhurin,[2,3] Cristiano Tolomei,[1] Andrea Antonioli[1] and Giuseppe Pezzo [1]

[1] *Istituto Nazionale di Geofisica e Vulcanologia, Osservatorio Nazionale Terremoti, Roma, Italia. E-mail: nikos.svigkas@ingv.it*
[2] *Institute of Volcanology and Seismology, Far East Branch of Russian Academy of Sciences, Petropavlovsk-Kamchatsky, Russia.*
[3] *Geological Institute, RAS, Moscow, Russia*

Accepted 2023 March 24. Received 2023 February 27; in original form 2022 December 21

SUMMARY

On the 9th of January 2020, an M_w 6.4 strike-slip earthquake took place north of the Asian margin of the Bering Sea. The earthquake occurred within the known reverse-right-lateral active fault zone, called Khatyrka–Vyvenka, which transverses the Koryak Highland from SE to NW and is thought to be a surface manifestation of the Asian portion of either the Bering plate boundary or the northern edge of the Alaskan stream. No other strong earthquake has ever been recorded in this remote uninhabited area and the few existing seismic stations provide poor quality earthquake locations. We adopt SAR interferometry (InSAR) technique to define an improved location of the Koryak 2020 earthquake and constrain the seismic source. The analysis of the 2020 event revealed a previously unknown active fault of left-lateral kinematics that is possibly hidden and strikes NW transversely to the Khatyrka–Vyvenka fault zone. Although several mechanisms could account for left-lateral kinematics of this fault, we propose that the structure is part of a more extended NW fault structure, that formed in pre-neotectonic times and has played a role of a pre-existing rheological discontinuity. This revived NW structure together with a similar structure located easterly, so far aseismic, make the plate/stream boundary segmented, step-like in plan view. The step-like boundary geometry may be the result of internal transform deformation of a rigid plate, but it is better explained by deflections of the Alaskan stream edge at local crustal asperities, which are pre-Cenozoic terrains.

Key words: Plate motions; Radar interferometry; Satellite geodesy; Seismic cycle; Asia; Seismicity and tectonics.

INTRODUCTION

The Koryak Highland lies to the north of the Kamchatka Peninsula, in NE Asia (Fig. 1). The area is mostly uninhabited, with only few sparse settlements. The continental crust of Koryakia was formed in the Mesozoic–Palaeogene when terranes moving from the Pacific Ocean collided with the Asian margin (Lander *et al.*1993, and references therein). By the age of the intermountain depression deposits, the formation of the orogenic structure of the Koryak Highland and the deformation of the pre-orogenic surface began around the Miocene (Geological map of Russia & adjoining water aeries 2004; Razumny *et al.*2017).

Two models have been proposed to describe the current plate setting of the region (Fig. 1). One is the model of the rigid Bering plate rotating clockwise relative to the pole located in Chukotka (Lander *et al.*1993; Mackey *et al.*1997), which implies predominantly thrust motions on the Koryak segment of the Bering plate boundary. The second is the model of the 'North Pacific Rim orogenic Stream' (here and below, referred to as the Alaska Stream for short) moving westward from Alaska (Redfield *et al.*2007). In this interpretation, the right-lateral motions along the Koryak segment of its boundary should probably dominate. In both models, the plate and the stream boundaries in Koryakia coincide with the Khatyrka–Vyvenska fault zone of active faults.

On the 9th of January 2020, an M_w 6.4 strike-slip event took place at Koryak Highland, a low seismicity area. The epicentral zone of the 2020 earthquakes is located in the place where major faults of the Khatyrka–Vyvenka zone make a left step (Fig. 1). Previous strong seismicity in the broader area was manifested by the 1991 M_w 6.6 Khailino earthquake and the 2006 M_w 7.6 Olyutor earthquake, both south-west of the 2020 event (Fig. 1). Mechanisms of both earthquakes show mainly reverse movements along the faults

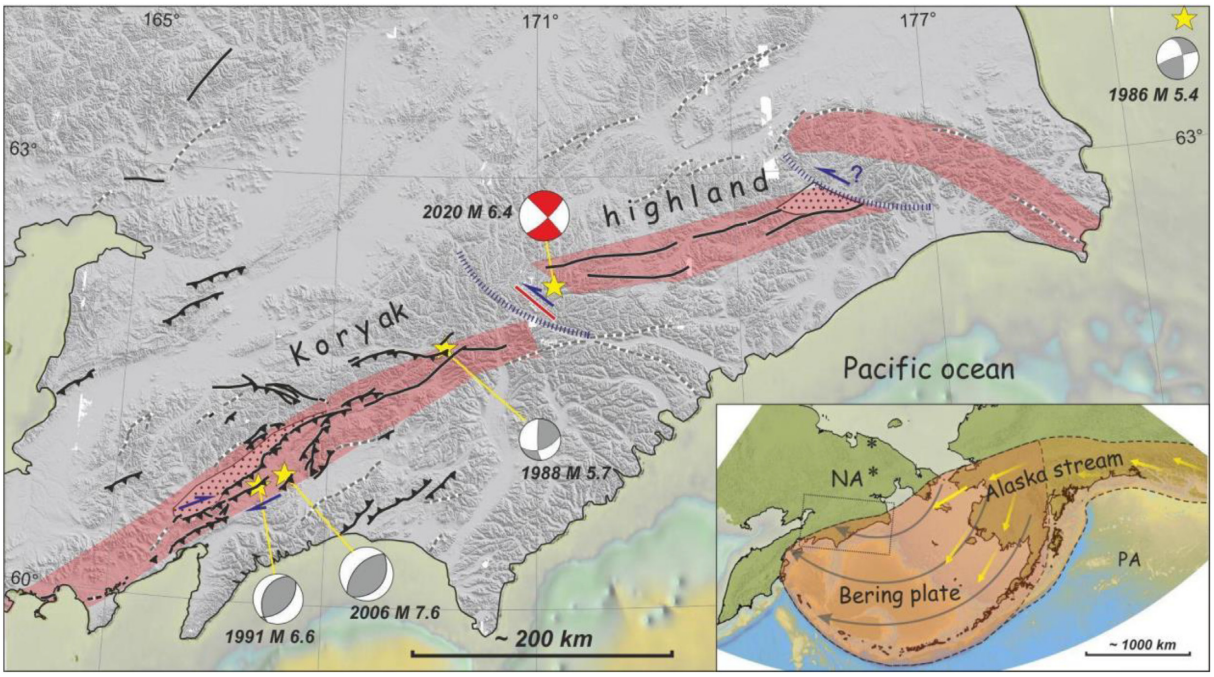

Figure 1. Active faults and main earthquake events in the Koryak Highland area. Black solid and dashed lines are reliable and inferred active faults of the Khatyrka–Vyvenka zone, respectively (http://neotec.ginras.ru/database.html and this study). Accompanying triangles and one-sided arrows indicate reverse and strike-slip components of fault movements. NW-striking red line in the centre is the 2020 fault (this study), and red-and-white solution is for the 2020 event. Curved blue cross-hatched strips mark west limits of pre-neotectonic terrains (Lander *et al.*1993, see the text). Purple semi-transparent fill covers segments of the Khatyrka–Vyvenka zone. Inset shows extents of Alaska stream (yellow semi-transparent fill, by Redfield *et al.*2007) and Bering plate, coinciding with western part of the stream (greyish yellow fill, by Lander *et al.*1993; Mackey *et al.*1997). Asterisks are poles of Bering plate rotation, by Lander *et al.* (1993, southern) and Mackey *et al.* (1997, northern). Grey and yellow arrows indicate directions of Bering plate and Alaska stream motion, respectively, in respect to North America Plate (NA). PA is Pacific plate. Shaded topography is generated from 100-m resolution Arctic Dem (http://data.pgc.umn.edu/elev/dem/setsm/ArcticDEM), and colour scaled bathymetry is derived from SRTM30 + data (Becker *et al.*2009).

with a minor right-lateral component, along nodal planes striking parallel to the zone (Global CMT catalogue: http://www.globalcmt.org/CMTsearch.html). The study of the 2006 Olyutor earthquake rupture (∼140 km length), revealed also reverse (south-east side up) and dextral movements (Rogozhin *et al.*2010). Earlier seismicity is manifested by the 1986 and 1988 events with strike-slip mechanisms (Dziewonski *et al.*1987, 1989).

InSAR (Interferometric Synthetic Aperture Radar) has become an important tool to measure the surface deformation over various phenomena (volcanoes, landslides, glaciers, aquifer activity, urban monitoring and earthquakes, e.g. Zebker & Goldstein 1986; Massonnet 1997; Massonnet & Feigl 1998; Galloway & Hoffmann 2007; Brencher *et al.*2021; Trasatti *et al.*2021; Funning et al 2005). The InSAR technique is ideal for studying remote areas where the field investigation, or the *in-situ* installation of other types of sensors, is difficult or impossible.

Right-lateral shearing along the NE part of the Khatyrka–Vyvenka zone is gradually replaced toward the southwest by compression (Lander *et al.*2010). This is the compression expressed during the Khailino and Olyutor earthquakes, though the latter demonstrated also some amount of dextral component as well.

Koryak is a region of sparse and tectonically ambiguous seismicity that makes this work a rare opportunity to study this specific part of the Khatyrka–Vyvenka zone, since no other strong earthquake has ever been recorded at the specific site. Only after the 1990s there was installation of seismic stations in the area (Lander *et al.*2010), therefore any previous recordings might potentially be incomplete or inaccurate. Identifying the actual geometry of the boundary zone is hard. Seismicity of the larger earthquakes ($M \geq 5$) can be seen in Fig. 2; the SW part has the major earthquake occurrences spanning down to a larger depth. Compared to this part, the NE part of the Khatyrka–Vyvenka zone, has a significantly lower seismicity during the instrumental period.

We exploit here radar satellite imagery to measure the surface deformation caused by the 2020 event, estimate an improved earthquake location and find which of the nodal planes is the causative fault. Based on geophysical modelling, we propose a plate tectonics interpretation of active faulting for the Koryak Highland area, in NE Asia.

METHODS

To find the earthquake's location and measure the surface deformation, we exploited SAR images from the Sentinel-1 (European Space Agency) and ALOS-2 (Japan Aerospace Exploration Agency) satellites. Acquisitions of both satellites from the ascending and descending orbits were exploited (Table 1). We adopted the InSAR technique (Massonnet & Feigl 1998) and the processing was performed through the SARscape (SARMAP, CH) software. We generated interferometric pairs, acquiring one image before and one image after the earthquake, to measure the co-seismic field surface displacement, along the satellite line-of-sight (LoS), that is, the line connecting the satellite to the ground pixel. For the removal of the topographic phase content, the ALOS world 3-D Digital Elevation

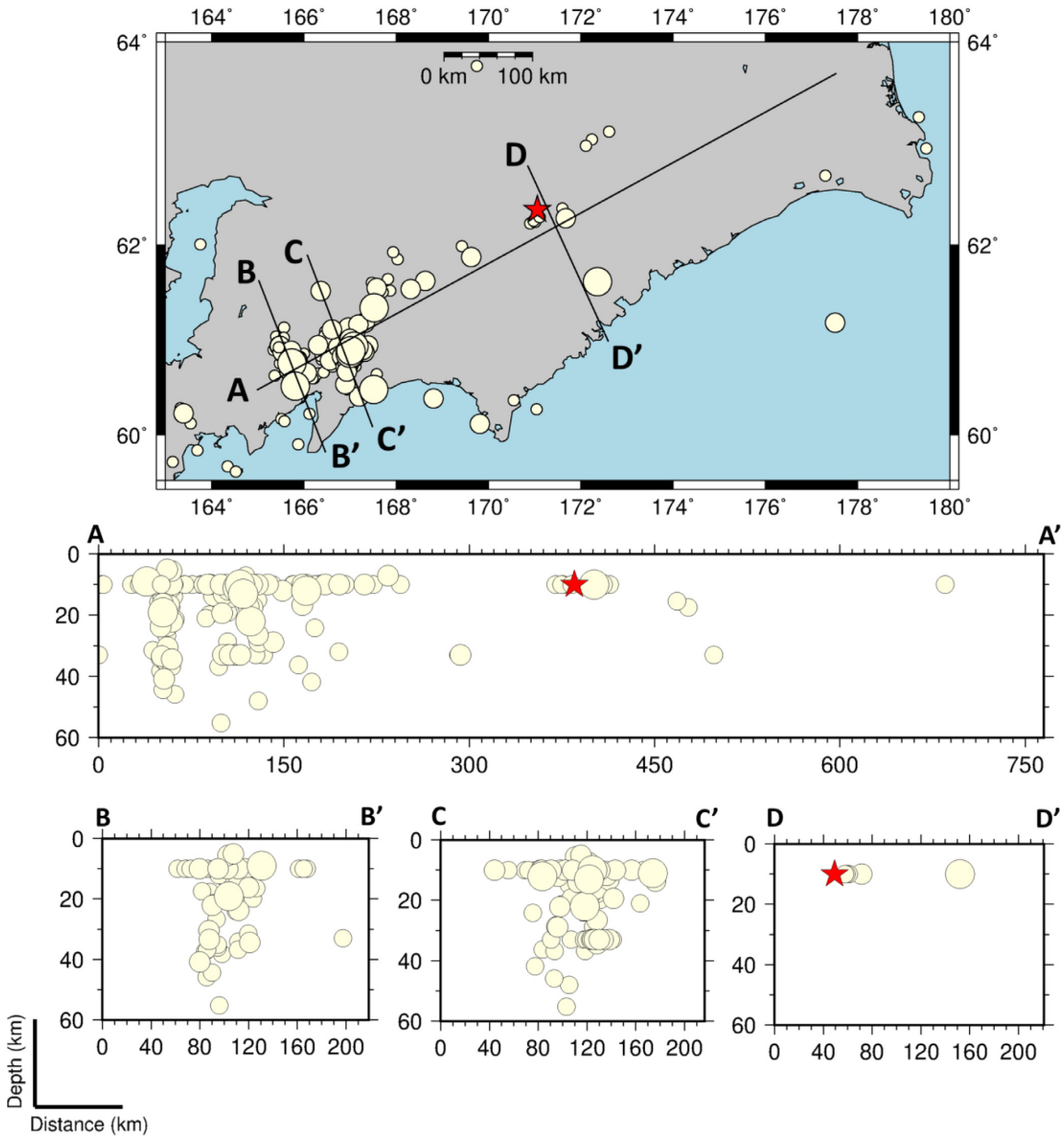

Figure 2. Seismicity $M \geq 5$ and cross-sections along the Khatyrka–Vyvenka zone. The star is the 2020 event. Most earthquakes have occurred at the SW part, whereas from the middle-to-NE part of the zone, the seismicity is significantly decreased.

Table 1. Radar Satellite data exploited and rms values of the linear inversion.

Satellite	Pre-event	Post-event	Δt (d)	Satellite pass	Rms linear inversion (m)
ALOS-2	11/07/2019	11/06/2020	336	Ascending	0.024
Sentinel-1	06/01/2020	18/01/2020	12	Descending	0.012
Sentinel-1	03/01/2020	15/01/2020	12	Descending	0.010
Sentinel-1	23/12/2019	16/01/2020	24	Ascending	0.015

Model (DEM) was used. The Goldstein filtering was applied (Goldstein &Werner 1998) and the unwrapping was performed by means of the minimum-cost flow approach (Costantini 1998).

We then used the estimated surface deformation results, to infer the seismic source that caused the event through data inversion, applied to a subset of points sampled from the unwrapped LoS interferograms. The selection of points used in the inversions was carried out with a regular sampling with two different resolutions: one point every 200 m in the near-field area and every 500 m in the far-field (Fig. S1, Supporting Information). The inversion strategy

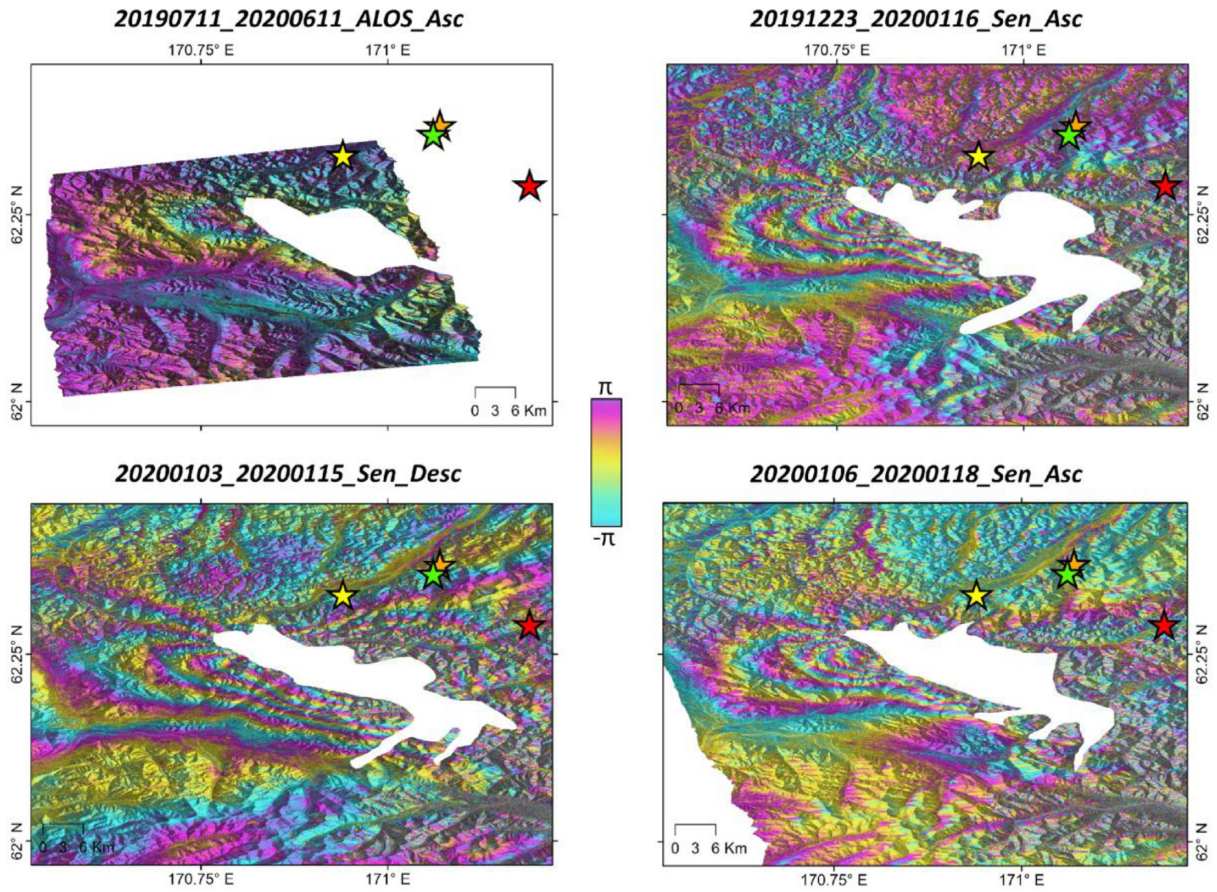

Figure 3. InSAR LoS surface displacements of the Koryak 2020 sequence. Stars are the epicentre locations from different agencies. Yellow: GFZ—GeoForschungsZentrum, green: USGS—United States Geological Survey, orange: GSRAS—Geophysical Service of the Russian Academy of Sciences and red: EMSC—European-Mediterranean Seismological Centre. Above each interferogram are the satellite acquisition dates; these follow the notation yyymmdd. Asc and Desc stand for the ascending and descending passes, respectively.

Table 2. Inversion results together with the 1σ uncertainties.

Nonlinear inversion	
Moment magnitude (N·m)	3.87E + 18
Average slip (m)	0.79 (±0.047)
Strike°	304 (±0.67)
Dip°	86 (fixed)
Rake°	−3.21(±1.47)
Length(m)	17 777 (±350.3)
Width (m)	9163.4 (±1025.8)
Depth (m)	189 (±81.3)
Longitude (deg)	170.9312 (±176.1 m)
Latitude (deg)	62.2140 (±138.8 m)
Linear inversion	
Moment magnitude (N·m)	4.37E + 18
Max slip (m)	2.1

follows a consolidated two-step approach; the first inversion consists of a nonlinear optimization to get the parameters of a uniform dislocation for a finite rectangular source, that is, location (latitude, longitude and depth), dimension (length and width), orientation (strike and dip angles), rupture direction (rake angle) and intensity (slip). This optimization is based on the Levenberg–Marquardt algorithm (Levenberg 1944; Marquardt 1963), implemented with multiple restarts starting from random configurations to avoid the least-square cost-function fall into a local minimum (see Atzori *et al.*2009 for details about the algorithm implementation).

For the best-fitting source obtained through nonlinear inversion, we also estimated the uncertainty of the free parameters; this was

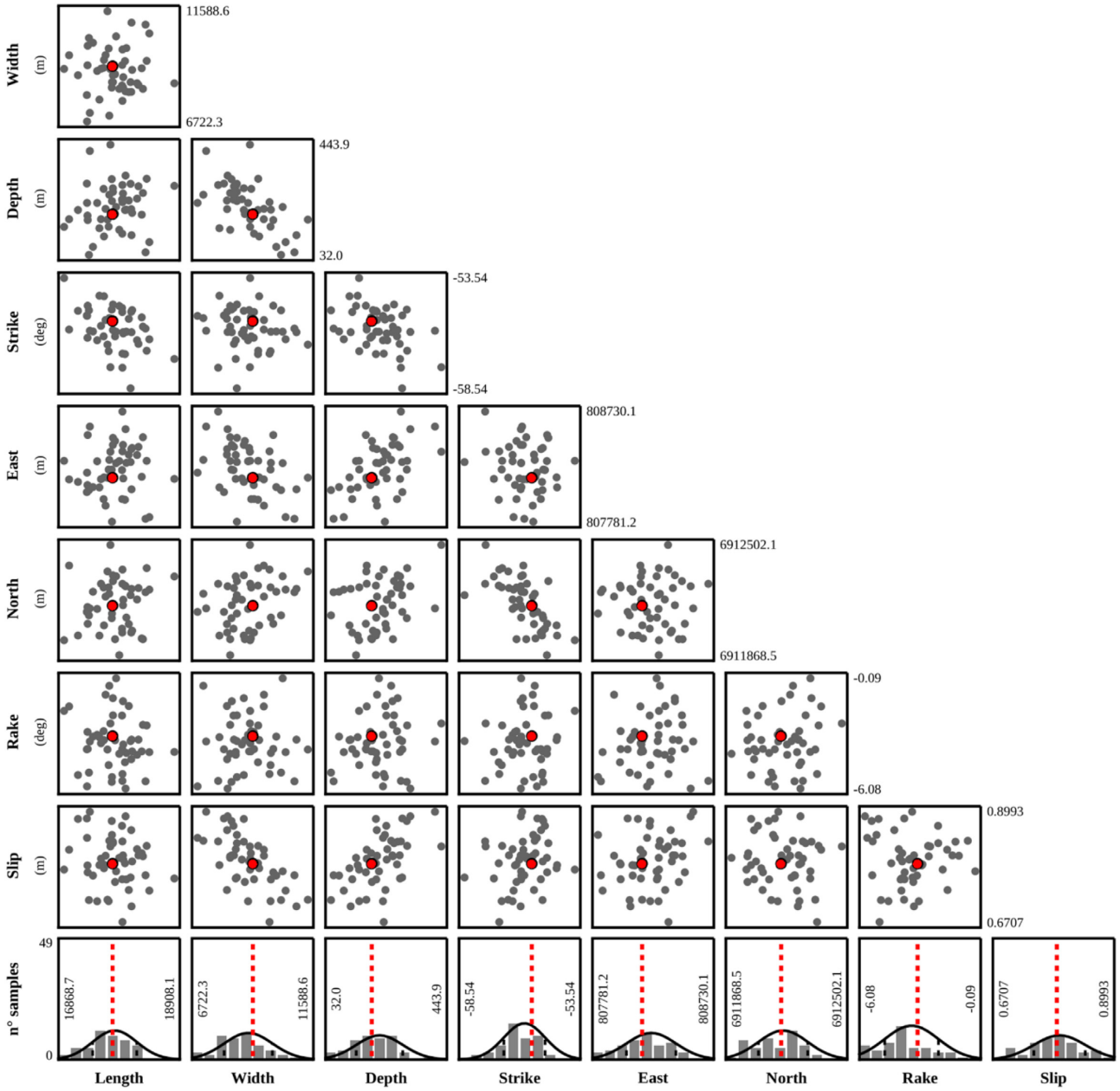

Figure 4. Trade-offs (scatter plots) and probability distributions (bottom row) for the nonlinear inversion of the Koryak 2020 event (red points and dashed lines indicate the best-fitting values).

done by performing a multiple number of nonlinear inversions after contaminating InSAR data sets with an *ad-hoc* noise, correlated in space. More specifically, we followed the empirical approach of starting from the full variance/covariance matrix of the observed data Cov(**d**) and then estimating a Cholesky decomposition of it, such that:

$$Cov\,(\mathbf{d}) = \mathbf{L}\mathbf{L}^{\mathrm{T}}$$

Then the synthetic noise data set, characterized by the same InSAR covariogram, was obtained from:

$$\mathbf{d}_{\mathrm{noise}} = \mathbf{L}\mathbf{d}_{\mathrm{GAUSS}}$$

where $\mathbf{d}_{\mathrm{GAUSS}}$ is a vector of uncorrelated Gaussian noise. Details can be also found in Parsons *et al.* (2006). This approach allows us to identify the existence of possible trade-offs between pairs of inverted parameters.

An important factor to take into account was the weighting coefficient w_D that represents the contribution of each one of the data sets simultaneously inverted. At the beginning of the procedure the w_D was assumed to be 1. Also, the cost function of the data, CF(D), was supposed to be 1. Nevertheless, this should happen only in theory, since a perfect estimation of Cov(**d**) is not attainable. To estimate the pragmatic values of w_D for each data set, we run the inversion procedure more than once. At first w_D was estimated based on the assumption:

$$\mathrm{CF}\,(D)\ w_D = 1$$

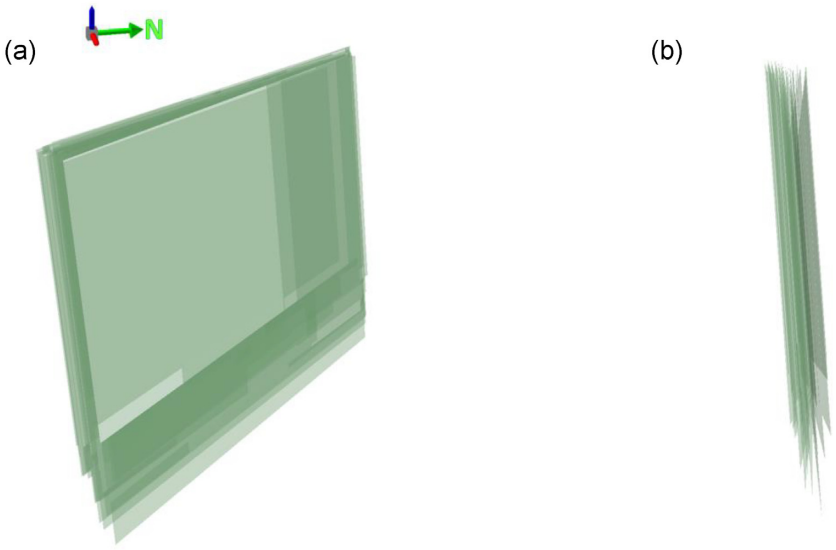

Figure 5. Visual representation of the uniform slip sources derived during the uncertainty analysis of the nonlinear inversion. (a) Oblique view and (b) side view.

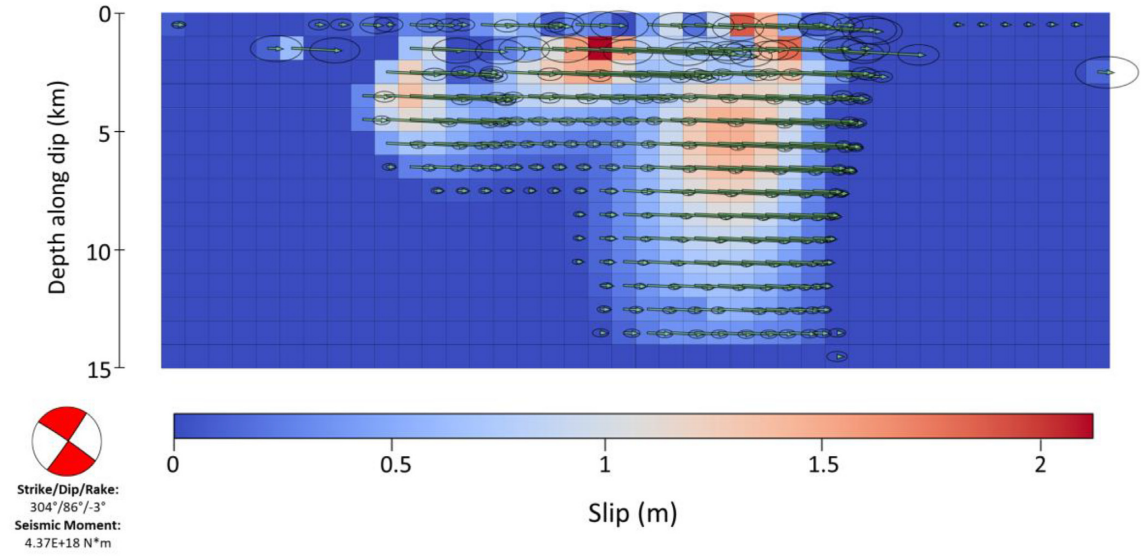

Figure 6. Slip distribution of the Koryak 2020 event with the rake arrows and the sigma ellipses. At the bottom left is the corresponding focal mechanism.

Then, a subsequent estimation of $w_D$was performed deriving from:

$$\mathrm{Cov}\ (\mathbf{d}_{\mathrm{new}}) = \frac{1}{w_D}\ \mathrm{Cov}\,(\mathbf{d})$$

where w_D acts as a stretching factor. After a few runs of the inversion w_D value gets stabilized indicating a balance in the contribution of the data sets (Atzori *et al.*2019).

The second inversion exploited the best-fitting source retrieved in the previous task to get the slip distribution over the fault, opportunely extended to allow the rupture vanish to zero at the edges and subdivided into patches of equal size. This was carried out with a linear inversion (Atzori *et al.*2019). The system of equation strategy we followed is described as :

$$\begin{bmatrix} \mathbf{d} \\ 0 \end{bmatrix} = \begin{bmatrix} \mathbf{G} \\ \varepsilon\ \nabla^2 \end{bmatrix} \mathbf{m}$$

where, $\mathbf{G}$ is the Green's functions matrix, ∇^2 is the Laplacian operator, tuned with the empiric damping factor ε (obtained by trial-and-error, as from Menke 1989), $\mathbf{d}$ are the InSAR data, extended with zeros for the appended part concerning the Laplacian operator and $\mathbf{m}$ is the slip vector retrieved by inversion. To prevent backslip, a non-negative least-squares scheme is adopted. For both nonlinear and linear inversions, the parameters of an orbital ramp are contextually estimated for each InSAR data set.

For the uncertainty estimation of the linear inversion, we applied the standard rules for error propagation:

$$\mathrm{Cov}\,(\mathbf{m})\ = \mathbf{G}^{-g}\ \mathrm{Cov}\,(\mathbf{d})\,\mathbf{G}^{-\mathrm{gT}}$$

where Cov($\mathbf{d}$) is the full variance-covariance matrix of the geodetic data and Cov($\mathbf{m}$) that of the m array. For the estimation of Cov($\mathbf{d}$) we made an analysis of the power spectra of a displacement map which contains only noise and artefacts. Based on this, the scattered plot of the covariance vs distance scatter plot was fitted. Details of

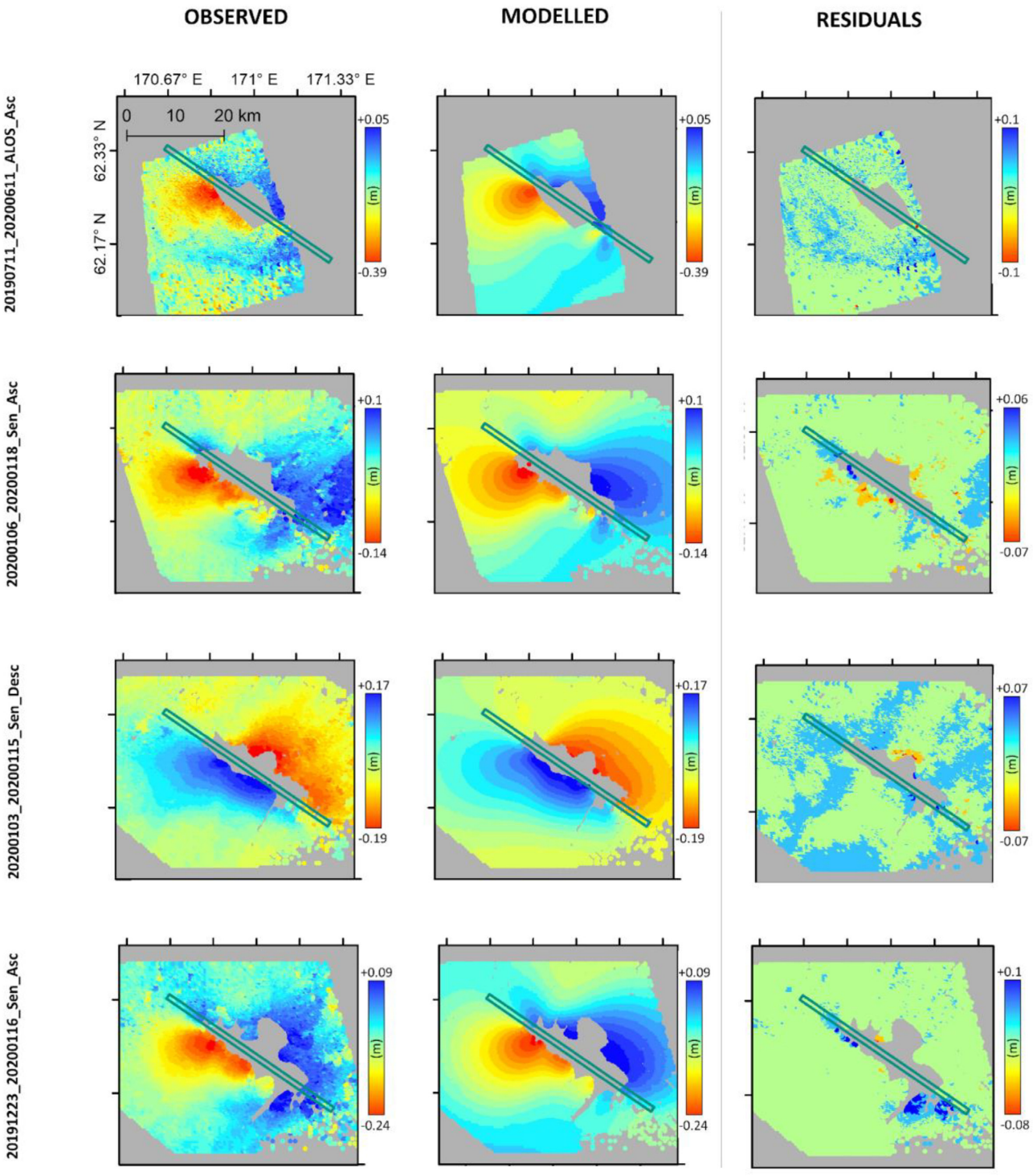

Figure 7. Comparison between observed and modelled surface displacement. The petrol green rectangle is the causative fault.

the procedure can be found in Atzori *et al.* (2009, 2019) and Atzori & Salvi (2014).

RESULTS

The interferograms (Fig. 3), excluding the area affected by low coherence, indicate a surface deformation with a maximum value of 46 cm. In the nonlinear inversion, we assumed that the fault is NW-SE oriented, as clearly visible from the interferometric fringe shape. This resolves the ambiguity between the two solutions provided by focal mechanisms. With the nonlinear inversion, InSAR data sets were able to constrain all the source parameters apart from the dip, which was unrealistically low and was therefore fixed to the value obtained from the Global Centroid Moment Tensor (GCMT) catalogue. The inversion results indicate a nearly vertical strike-slip structure with strike°, dip° and rake°: 304°, 86° and −3°, respectively. These describe a nearly pure left-lateral rupture, with an average uniform slip of 0.8 m over roughly a 18 by 9 km

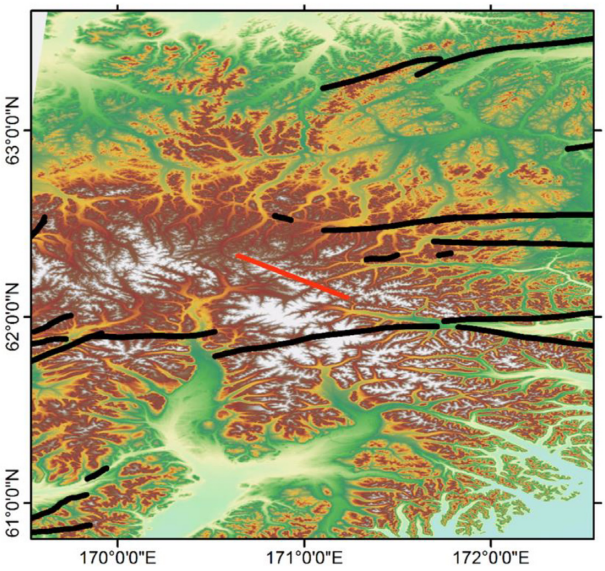

Figure 8. Fault map of the area, black lines are the already known faults. Red rectangle is showing the Koryak 2020 strike-slip seismic source.

fault, corresponding to a seismic moment release of 3.87E + 18 N·m (Table 2). The uncertainty analysis of the free parameters in the non-linear inversion is shown with the scattered plots and probability distributions in Fig. 4. It can be noted that all parameters were well constrained and there is no evidence of strong trade-offs. A visual representation of the uniform slip sources derived from the non-linear inversion uncertainty analysis, showcases a well-constrained source, in terms of geometry (Fig. 5). The slip distribution, derived from the linear inversion shows an interesting pattern with four distinct slip peaks and a maximum value of about 2.1 m (Fig. 6). The largest slip patch reached the depths of about 14 km, covered an area of 7 × 13 km. The error ellipses shown on the slip distribution are the parameter variances. Geodetic magnitude was estimated to be M_w 6.39. The optimum model presented here can predict well the observed deformation (Fig. 7) with root mean square (rms) values of the linear inversions showed in Table 1. In order to evaluate whether the slip distribution is compliant with the resolution permitted by data, we also exploited the 'full resolution' method developed by Atzori & Antonioli (2011): the fault is automatically subdivided into patches of variable size according to the real data ability of spatially resolving details on the fault. Our result validates the proposed Koryak 2020 regular patches slip distribution results, showing a similar identification of the slip peaks (Supporting Information).

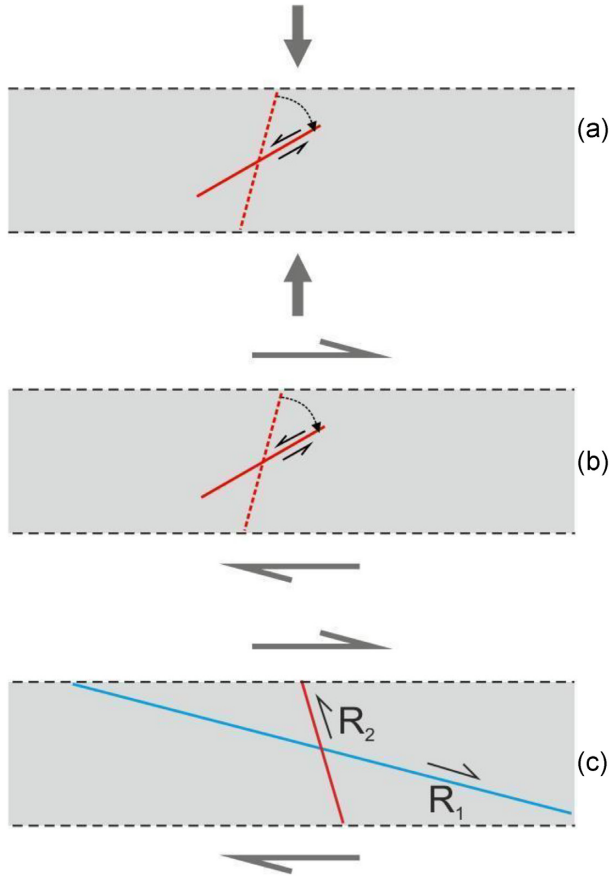

Figure 10. Possible causes of horizontal movements along the 2020 fault: (a) and (b)—rotation of a fault plane due to either shortening (a) or shearing (b) ('domino' model), dashed line indicate the initial position of a fault plane, (c)—the fault is Riedel$_2$ shear within a right-lateral zone (e.g. Scholz 2002).

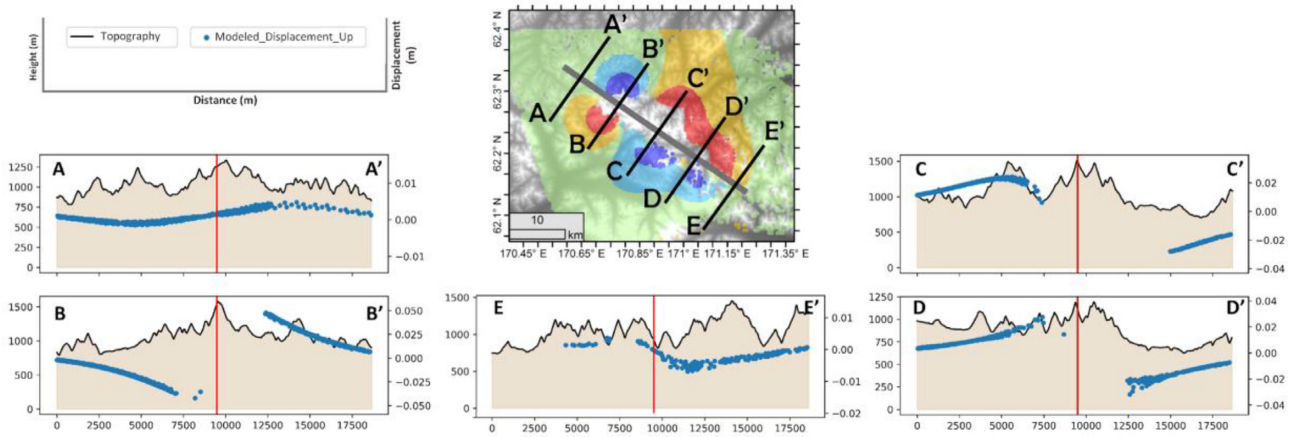

Figure 9. Topography and predicted vertical deformation along the Koryak 2020 source. A–A′, B–B′, C–C′, D–D′, E–E′ are the topographic line profiles presented in the graphs. Blue dots are the modeled displacements in the vertical component, black lines is the topography and red vertical lines in the graphs are showing the location of the Koryak 2020 causative fault.

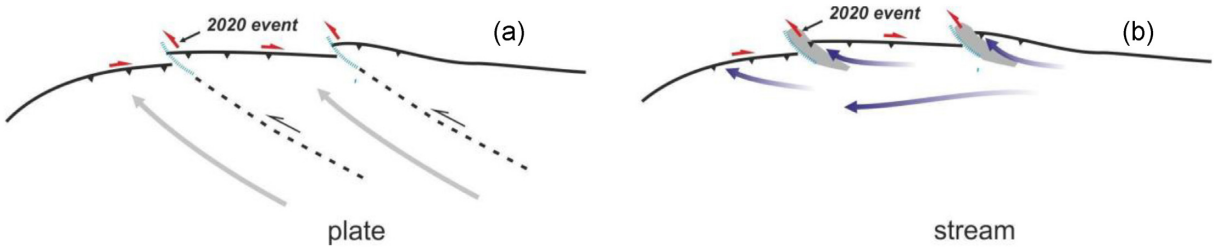

Figure 11. Cartoons illustrating probable causes of step-like geometry of the Khatyrka–Vyvenka fault zone (bering plate boundary or the edge of the Alaska stream). In (a), dashed lines are transform faults parallel to the vectors of plate motion. In (b), violet lines are inferred directions of stream flow, grey areas mark terrains.

DISCUSSION

The area of the Koryak 2020 main shock lies in a region of rather sparse recorded seismicity. Spatial offsets of earthquake locations estimated from seismology and geodesy had been previously highlighted in the literature (e.g. Lohman & Simons 2005). Results shown here indicate an offset distance of the 2022 epicentre of about 8–18 km away from the real location of the event (Fig. 3). The event occurred on a previously unknown active fault (Fig. 8). It is not clear whether this structure is related with obvious topographic features (Fig. 9), thus we leave open the possibility to have a hidden fault (e.g. Pezzo *et al.*2014).

There is a gap in the Khatyrka–Vyvenka active fault zone, the northern boundary of the plate or stream, coinciding approximately with the highest part of the Koryak Highland. Relative to the gap, the zone is offset in plan with a left-lateral step. The 2020 fault is located in this gap and extends at an oblique angle to the Khatyrka–Vyvenka fault zone (Fig. 1).

The 2020 fault cannot be a conjugate because there is no main fault in relation to which it could be. The left-lateral displacements along the 2020 fault also cannot be the result of rotation of its plane, neither under the transverse contraction of the zone nor under the predominantly right-lateral movements along it. In both schemes, the fault should strike NE-SW (Figs 10a and b). In principle, the revealed fault can be interpreted as a Riedel-2-type element in the right-lateral strike-slip zone (e.g. Scholz 2002) (Fig. 10c), but this interpretation implies continuity of the right-lateral strike-slip zone, which in the case of the Khatyrka–Vyvenka zone is not observed.

The northwest-trending pre-KZ Ukelayat fault stretches within the gap in the Khatyrka–Vyvenka zone. The fault is close to the west bound of an uplift with outcrops of Jurassic sediments among the Cretaceous (Razumny *et al.*2017), which is correlated with one of the pre-Cenozoic terrains of the region (see Lander *et al.*1993). The idea that the uplift, as crust heterogeneity, could have prevented the spreading of active strike-slip faults of the Khatyrka–Vyvenka zone was first suggested by A. V. Lander (personal communication 2021). It should be noted that a similar NW-trending, zone limiting another pre-Cenozoic terrane may be distinguished to the east (see Fig. 1). Relative to it, the system of presumably active faults is also displaced left-laterally. Thus, the segmentation of the Koryak part of the Bering Plate boundary or the stream edge seems to be a rule rather than an exception. The significance of the 2020 event is that it manifested the existence of transverse zones as active (at least one of them) and their left-lateral kinematics.

The structural and geodynamic interpretation of the transverse zones depends on the choice between a rigid plate (Bering Plate) and extruded mobile crust (the Alaska stream). In the variant with a rigid plate, the transverse zones are parallel to the vector of its motion, have the character of transform and, most importantly, should extend inside the plate, with no evidence for this (Fig. 11a). The variant with a stream seems simpler and, therefore, more appropriate. It does not require the existence of local transform deformations: the appearance of transverse left-lateral strike-slip zones may be just a response of the stream edge to the occurrence of upper Earth's crust heterogeneities (Fig. 11b).

CONCLUSIONS

Geodetic analysis of the 2020 M_w 6.4 Koryak event revealed a previously unknown possibly hidden left-lateral fault of the NW strike, transverse to the major Khatyrka–Vyvenka SW-NE region of active faults in the Koryak Highland area.

Comparison of the 2020 fault with the pre-neotectonic geological structure shows that it may be an element of an extended fault zone, limiting one of the pre-Cenozoic terrains of the region from the southwest. A similar zone, with no events detected yet, also exists to the east. Both zones divide the Khatyrka–Vyvenka active fault zone, interpreted as the northern boundary of the Bering Plate or the northern edge of the Alaska stream, into segments arranged as *echelon* geometry (with left-stepping).

The segmentation and *en echelon* arrangement of segments of the Khatyrka–Vyvenka fault zone seems to be better and more easily explained by the deviation of the Alaska stream edge on crustal heterogeneities. If we talk about rigid plates, then, in principle, the stepped geometry of their boundaries represents an exceptionally rare case. Such geometry of the plate boundaries is characteristic mainly for their spreading sections. In the case of the Bering Plate, its northern boundary segmentation and segment *en echelon* arrangement suggest the presence of transform faults inside of it, evidence of which is lacking.

ACKNOWLEDGMENTS

European Space Agency and Copernicus EU are thanked for the provision of Sentinel-1 images. ALOS-2 data were obtained courtesy of the JAXA agency in the framework of the Earth Observations Collaborative Research Agreement between the Japanese Aerospace Exploration Agency and the Research Organization (no. ER2A2N173A). Part of the figures were created with generic mapping tools (GMT, http://gmt.soest.hawaii.edu/). In this study, the ALOS DEM data were used: ALOS DEM data Japan Aerospace Exploration Agency (2021). Seismicity data are from the Unites States Geological Survey (USGS). ALOS World 3D 30 meter DEM. V3.2, 2021 January. Distributed by OpenTopography, https://doi.org/10.5069/G94M92HB. Some of the active faults shown

are from Active Faults of Eurasia Database (AFEAD, Zelenin *et al.*2022). NS acknowledges support by the Italian Ministry of Economic Development (MISE) under the MISE DGISSEG-INGV 2020 project contract.

DATA AVAILABILITY

Satellite data used are available from the European Space Agency (ESA) and Japan Aerospace Exploration Agency (JAXA).

REFERENCES

Atzori, S. *et al.* 2009. Finite fault inversion of DInSAR coseismic displacement of the 2009 L'Aquila earthquake (central Italy), *Geophys. Res. Lett,* **36**(15), L15305. doi: 10.1029/2009GL039293.

Atzori, S. & Antonioli, A., 2011. Optimal fault resolution in geodetic inversion of coseismic data, *Geophys. J. Int.,* **185,** 529–538.

Atzori, S., Antonioli, A., Tolomei, C., Novellis, V, Luca, C. & Monterroso, F., 2019. InSAR full-resolution analysis of the 2017–2018 M>6 earthquakes in Mexico, *Remote Sens. Environ.,* **234,** 111461. doi: 10.1016/j.rse.2019.111461.

Atzori, S. & Salvi, 2014. SAR data analysis in solid Earth geophysics: from science to risk management http://dx.doi.org/10.5772/57479.

Becker, J.J. *et al.*, 2009. Global bathymetry and elevation data at 30 arc seconds resolution: SRTM30_PLUS, *Mar. Geod.,* **32**(4), 355–371.

Brencher, G., Handwerger, A. L. & Munroe, J. S., 2021. InSAR-based characterization of rock glacier movement in the Uinta Mountains, Utah, USA, *The Cryosphere,* **15,** 4823–4844. https://doi.org/10.5194/tc-15-4823-2021.

Costantini, M., 1998. A novel phase unwrapping method based on network programming, *IEEE Trans. Geosci. Remote Sens.,* **36**(3), 813–821.

Dziewonski, A M., Ekstrom, G., Woodhouee, J.H. & Zwart, G., 1987. Centroid-moment tensor solutions for October-December 1986, *Phys. Earth planet. Inter.,* **48,** 5–17.

Dziewonski, A.M., Ekstrom, G., Woodhouse, J.H. & Zwart, G., 1989. Centroid-moment tensor solutions for October-December 1988, *Phys. Earth planet. Inter.,* **57,** 179–191.

Funning, G.J., Parsons, B., Wright, T.J., Jackson, J.A. & Fielding, E.J., 2005. Surface displacements and source parameters of the 2003 Bam (Iran) earthquake from Envisat advanced synthetic aperture radar imagery, *J. geophys. Research: Solid Earth,* **110,** B9. doi: 10.1029/2004JB003338.

Galloway, D.L. & Hoffmann, J., 2007. The application of satellite differential SAR interferometry-derived ground displacements in hydrogeology, *Hydrogeol. J*., **15,** 133–154. https://doi.org/10.1007/s10040- 006-0121-5

Geological map of Russia and adjoining water aeries, scale 1: 2 500 000, 2004. *Ministry of Natural Recourses of the Russian Federation,* (Petrov, O.V., Editor in Chief). Cartographic Office of VSEGEI.

Goldstein, R.M. & Werner, C.L., 1998. Radar interferogram filtering for geophysical applications, *Geophys. Res. Lett.,* **25,** 4035–4038.

Lander, A.V., Levina, V.I. & Ivanova, E.I., 2010. The earthquake history of the Koryak Upland and the aftershock process of the *MW* 7.6 April 20(21), 2006 Olyutorskii Earthquake ISSN 07420463, *J. Volc. Seismol.,* **4**(2), 87–100.

Lander, A.V., Bukchin, B.G., Droznin, D.V. & Kiryushin, A.V., 1993. Tectonic position and source parameters of the Khailin (Koryak) earthquake of March 8, 1991: does the Beringia plate exist?. *Vychislitel'naya seismologiya (Computational Seismology).,* **26**. Moscow: Nauka, pp. 103–122. (in Russian).

Levenberg, K., 1944. A method for the solution of certain problems in least squares, *Quarterly of applied mathematics,* **2**(2), 164–168.

Lohman, R.B. & Simons, M., 2005. Locations of selected small earthquakes in the Zagros mountains, *Geochem. Geophys. Geosys,* **6,** Q03001, doi:10.1029/2004GC000849 .

Mackey, K.G., Fujita, K., Gunbina, L.V., Kovalev, V.N., Imaev, V.S., Koz'min, B.M. & Imaeva, L.P., 1997. Seismicity of the Bering Strait region: evidence for a Bering block, *Geology,* **25**(11), 979–982

Marquardt, D., 1963. An Algorithm for Least-Squares Estimation of Nonlinear parameter., *SIAM Journal on Applied Mathematics,* **11**(), 431–441.

Massonnet, D. & Feigl, K.L., 1998. Radar interferometry and its application to changes in the earth's surface, *Reviews of Geophysics,* **36**(4), 441–500.

Massonnet, D., 1997. Satellite radar interferometry, *Sci. Am.,* **276**(2), 46–53.

Menke, W., 1989. *Geophysical Data Analysis: Discrete Inverse Theory,* (Academic Press).

Parsons, B. *et al.*, 2006. The 1994 Sefidabeh (eastern Iran) earthquakes revisited: new evidence from satellite radar interferometry and carbonate dating about the growth of an active fold above a blind thrust fault, *Geophys. J. Int.,* **164,** 202–217.

Pezzo, G., Merryman Boncori, J.P., Atzori, S., Antonioli, A. & Salvi, S, 2014. Deformation of the western Indian Plate boundary: insights from differential and multi-aperture InSAR data inversion for the 2008 Baluchistan (Western Pakistan) seismic sequence, *Geophys. J. Int.,* **198,** 25–39.

Razumny, A.V. *et al.*, 2017. State geological map of Russian Federation. Scale 1:1 000 000 (third generation). Koryak-Kurile series. Sheet *P*-59 – Pakhachi. Explanatory note, *Saint-Petersburg, Cartographic Office of VSEGEI,* 323p.

Redfield, T.F., Scholl, D.W., Fitzgerald, P.G. & Beck, M.E., Jr., 2007. Escape tectonics and the extrusion of Alaska: past, present, and future, *Geology,* **35**(11), 1039–1042.

Rogozhin, E. A., Ovsyuchenko, A. N., Marakhanov, A. V. & Novikov, S. S., 2010. Geological study of the epicentral area of the April 20(21), 2006 Olyutorskii Earthquake, *Volcanol. Seismol.,* **4**(2), 79–86.

Scholz, Ch.H., 2002. *The Mechanics of Earthquakes and Faulting*(second edition). Cambridge University Press, 471p.

Trasatti, E, Tolomei, C, Wei, L & Ventura, G, 2021. Upward magma migration within the multi-level plumbing system of the Changbaishan Volcano (China/North Korea) revealed by the modeling of 2018–2020 SAR data, *Front. Earth Sci.,* **9,** 741287, doi:10.3389/feart.2021.741287

Zebker, H.A. & Goldstein, R.M., 1986. Topographic mapping from interferometric synthetic aperture radar observations, *J. geophys. Res.,* **91,** 4993–4999.

Zelenin, E., Bachmanov, D., Garipova, S., Trifonov, V. & Kozhurin, A., 2022. The Active Faults of Eurasia Database (AFEAD): the ontology and design behind the continental-scale dataset, *Earth Syst. Sci. Data,* **14**(10), 4489–4503. doi: 10.5194/essd-14-4489-2022.

SUPPORTING INFORMATION

Supplementary data are available at *GJI* online.

Figure S1. Polygon shapefile (black lines) defining the sampling areas. Numbers indicate the sampling resolution (in m) in the near-field and the far-field. The red rectangle is the Koryak 2020 fault.
Figure S2. Comparison between the linear inversion results between a fault subdivision into patches with a pre-defined and equal size (left) and a fault subdivision driven by the model resolution matrix (right), according to the algorithm described in Atzori & Antonioli (2011).

Please note: Oxford University Press is not responsible for the content or functionality of any supporting materials supplied by the authors. Any queries (other than missing material) should be directed to the corresponding author for the paper.